Available online at www.sciencedirect.com
ScienceDirect
Ceramics International 35 (2009) 2311–2323
CERAMICS INTERNATIONAL
www.elsevier.com/locate/ceramint

The effect of high-energy ball milling parameters on the preparation and characterization of fluorapatite nanocrystalline powder

E. Mohammadi Zahrani, M.H. Fathi *

Biomaterials Group, Department of Materials Engineering, Isfahan University of Technology, Isfahan, 84156-83111, Iran

Received 18 August 2008; received in revised form 25 November 2008; accepted 16 January 2009
Available online 6 February 2009

Abstract

The aim of this work was to evaluate the effect of ball milling parameters on the synthesis of fluorapatite nanopowder; also, the effect of fluoridation on bioresorbability and bioactivity of apatite was studied. Fluoridated hydroxyapatite nanopowders with 100% (fluorapatite, FA) were synthesized via mechanical alloying method. The results showed that the size and number of balls had no significant effect on the synthesizing time and grain size of FA, while decreasing the rotation speed or ball to powder weight ratio increased synthesizing time and the grain size of FA. In vitro test indicated that the bioactivity of FA was less than HA since the dissolution rate, precipitation amount and the size of precipitated bone-like apatite crystals on the surface of FA samples was clearly lower than HA.

Keywords: A. Milling; B. Spectroscopy; D. Apatite; E. Biomedical application

1. Introduction

Synthetic hydroxyapatite (HA) is the most unique calcium phosphate that has been intensely studied over the recent years in the form of powder [1–3], coating [4,5] or composite [6,7] for different clinical applications involving repair of bone defects, bone augmentation, as well as coating for metallic implants; these medical applications have been developed for HA bioceramic due to its structural and compositional similarity to the mineralized matrix of natural bone [8]. However, high dissolution rate in biological environment, poor corrosion resistance in an acid environment and thermal decomposition as a result of poor chemical stability in high temperatures, have restricted the applications of HA [9]. Among these shortcomings, the biodegradation of HA under physiological conditions is the most important restricted factor which makes the interface between porous or dense HA and bone unstable. In addition, high dissolution rate presents a long-term performance problem of HA coatings on ceramic or metallic implants which are used for cases such as dental roots and fastening nails for fracture bones [10].

Biological HA as the main inorganic phase of human hard tissue, doped with different quantities of cations such as Na^+, K^+, Mg^{2+} and anions as CO_3^{2-}, SO_4^{2-} and F^{1-}. Among them, F^{1-} plays leading roles because of its influence on the physical and biological properties of HA [8]. In practice, F^{1-} itself has been widely investigated in dental restoration areas because it prevents dental caries in a bacteria containing, acid environment. In addition, F^{1-} itself promotes the mineralization and crystallization of calcium phosphate in the bone forming process [11]. Incorporation of fluorine into the apatite structure to form what is known as fluoridated hydroxyapatite [FHA: $Ca_{10}(PO_4)_6OH_{2-x}F_x$; where x stands for the degree of fluoridation] is helpful in improvement of the cited poor properties of HA in biomedical applications. Recently, fluorine-substituted hydroxyapatite has attracted much attention and has been increasingly investigated by different researchers as clinical restoration materials due to the extensive findings of fluoridated HA in the bone and teeth and favorable effects of fluoride ions on bone ingrowth [8]. In vitro results have shown that FHA could provide lower dissolution, better apatite-like layer deposition and better protein adsorption [10,12], comparable or better cell attachment in comparison with pure HA [10,13], improved alkaline phosphates activity [10] and significant impact of fluorine ions on proliferation, morphology and differentiation of osteoblast-like cells in cell culture [13,14].

* Corresponding author. Tel.: +98 311 3915708; fax: +98 311 3912752.
E-mail addresses: fathi@cc.iut.ac.ir, fathimoh@yahoo.com (M.H. Fathi).

0272-8842/$34.00
doi:10.1016/j.ceramint.2009.01.012

Also, FHA could sufficiently provide low levels of fluoride to act upon the surrounding cells for improving bone formation, while avoiding unnecessary accumulation within the body [15]. As a result, FHA has good potential as an alternative for pure hydroxyapatite in bioactive applications.

The synthesis of FHA, therefore, is of great value and has been widely investigated by multiple techniques, such as precipitation [9], sol–gel [16], hydrolysis [17], hydrothermal [18], pH cycling [19] processing routes and solid-state reactions [20]. However, most of the wet methods need the precise controls on the processing conditions and the composition and properties of final products, which are strongly influenced by various parameters. The procedure and the apparatus for these processes are complicated, also, post heat treatment and long time is necessary to obtain final products with stoichiometric composition and proper crystallinity. Thus, wet methods are not suitable for mass production especially in industrial scales [15].

The mechanical alloying (MA), as a solid-state simple method for powder preparation takes advantage of the perturbation of surface-bonded species through creating pressure to enhance thermodynamic and kinetic reactions between solids. Furthermore, in comparison with wet processes, MA approach has a great deal of well known inherent advantages because of its being both economical and technically simple to perform mass productivity and its tremendous flexibility to generate nanocrystalline powders [21]; hence, over the past decades, it has been widely developed for the fabrication of a wide range of ceramic materials [22,23]. However, it was well known that the presence of impurities in the final products as a result of wear between vial and balls has been the most important shortcoming of MA process. From this point of view, optimizing the MA parameters to synthesize a pure product which could satisfy the requirements of ASTM F1185-88 [24] specification to be used as a biomaterial is very important.

The aim of the present work was to synthesize fluorapatite nanopowder via mechanical alloying technique. The effect of ball milling parameters such as rotation speed, diameter and number of balls, ball to powder weight ratio and milling time on the synthesis of fluorapatite nanopowder were evaluated, as well. Moreover, the effect of fluoridation on the biological performance of the apatite nanopowder in terms of its dissolution behavior and in vitro bioactivity in SBF was investigated.

2. Experimental procedure

2.1. Preparation of nanopowders

Powders mixture of calcium hydroxide ($Ca(OH)_2$), phosphorous pentoxide (P_2O_5) and calcium fluoride (CaF_2) powders (all p.a., Merck) with appropriate amount of reagents, were mechanically alloyed using a high-energy planetary ball mill (Fretch Pulverisette-5, Germany) with 500 ml zirconia vial and zirconia balls at ambient temperature. SEM photomicrographs of $Ca(OH)_2$ and CaF_2 at different magnifications are shown in Fig. 1. The $Ca(OH)_2$ particles had an irregular/polyhedron shape with a size distribution of ~0.5–5 μm. CaF_2 particles were angular in shape with a close size distribution ranging from ~1 to 2 μm. MA process was performed under various milling times and different milling conditions including; series I–V in Table 1, in order to investigate the effect of MA parameters such as number and size of the balls, rotation speed, and powder to ball weight ratio on the synthesizing time, crystallite size and purity of final produced powders. The weight of initial powder mixture in all different conditions was constant, equal to 5.272 g. The time of milling was selected equal to 15, 30, 60 min, and 2, 4, 6, 8, 10, and 15 h. The designed degree of substitution of OH^{1-} by F^{1-} was indicated by the x value in the general formula of FHA ($Ca_{10}(PO_4)_6OH_{2-x}F_x$), where x value was selected equal to 0 and 2. The subsequent obtained powders were correspondingly named as FHA0 and FHA100. The molar ratio of calcium hydroxide to phosphorous pentoxide and calcium fluoride was 9:3:1 and 10:3:0 for x value equal to 2 and 0, respectively.

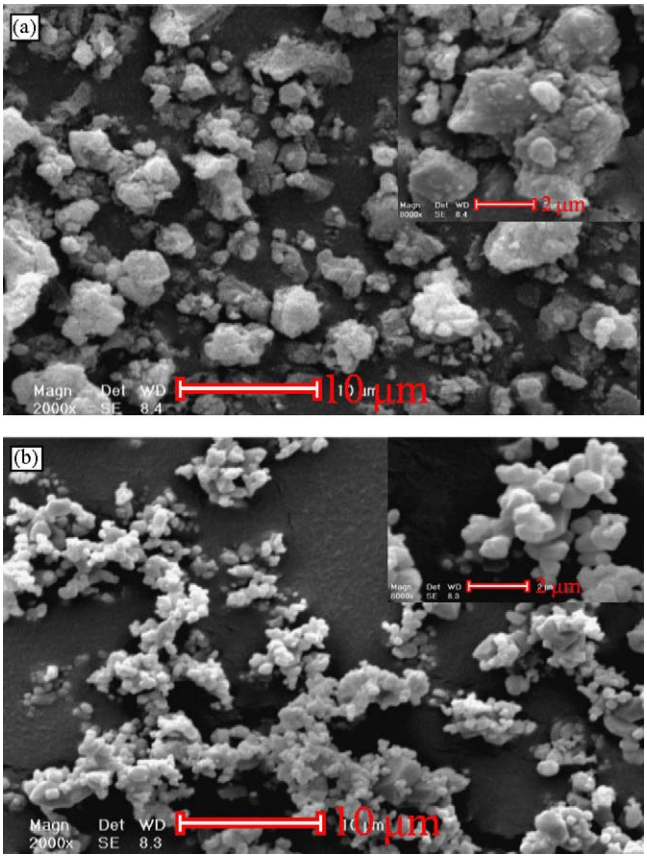

Fig. 1. SEM photomicrographs which show the morphology and agglomeration size distribution of the initial components: (a) $Ca(OH)_2$ and (b) CaF_2.

Table 1
Five different mechanical alloying conditions.

Parameter	Condition				
	I	II	III	IV	V
Ball/powder weight ratio	35	35	35	35	20
Rotation speed (rpm)	350	350	300	250	300
Number of balls	12	8	8	8	5
Diameter of balls (cm)	1	2	2	2	2

2.2. Characterization techniques

Phase structure analyses were carried out by X-ray diffractometer (XRD, Philips Xpert) using Ni filtered Cu Kα ($\lambda_{Cu\ K\alpha}$ = 0.154186 nm, radiation at 40 kV and 30 mA) over the 2θ range of 10–70°. The obtained experimental patterns were compared to standards compiled by the Joint Committee on Powder Diffraction and Standards (JCDPS). The FHA crystallite size and lattice strain was estimated with broadening XRD peaks by Williamson–Hall formula [25] (Eq. (1)).

$$B\cos\theta = \frac{0.89\lambda}{d} + \eta\sin(\theta) \quad (1)$$

where λ is wavelength of the X-ray (nm), B is the full width of diffraction peak under consideration (rad) in the middle of its height that was considered after computer-fit of the X-ray data using the Gaussian line shape, and θ is Bragg's angle (°). The crystallite size, d (nm), and the lattice strain, η could be calculated. The crystallite size determination of each sample was repeated twice for two groups of peaks; one group was (0 0 2), (2 1 1), (3 0 0) and another was (2 2 2), (0 0 4) and (2 1 3) Miller's planes family and the average of these two measurements was reported as crystallite size while typical standard deviation was 1–2 nm.

The functional groups of samples were analyzed with Fourier transform infrared spectroscopy (FTIR, Bomem, MB100) in a mid-IR spectrum range in the range of 400–4000 cm^{-1}. For this purpose each powder was mixed with KBr. The FTIR spectra were acquired with resolution of 2.0 cm^{-1}.

Transmission electron microscopy, TEM (Philips CM 200 FEG: Eindhoven, The Netherlands) operating at accelerating voltage of 200 kV, was utilized to study the morphology and to determine the size of nanoparticles after ball milling.

The morphology and agglomerate size distribution of the milled powders were investigated by scanning electron microscopy, SEM (Phillips XL 30: Eindhoven, The Netherlands).

Since the apatite lattice is well known to accommodate impurities, in order to evaluate the purity of synthesized powders, a trace element analysis was conducted with an inductively coupled plasma optical emission spectroscopy (ICP-OES: Jobin Yvon, Horiba Group) in a low resolution, high sensitivity mode to determine heavy metals as specified in ASTM F1185-88 standard, rare earth and other elements.

2.3. In vitro bioactivity evaluation

In vitro bioactivity of the obtained powders was investigated by soaking them in the simulated body fluid (SBF). The standard SBF solution was prepared according to Kokubo's protocol [26] by dissolving appropriate amount of the relevant reagent-grade chemicals in deionized water.

The inorganic ions concentrations in this standard SBF (Na^+ 142.0, K^+ 5.0, Mg^{2+} 1.5, Ca^{2+} 2.5, Cl^{1-} 147.8, HCO_3^{1-} 4.2, HPO_4^{2-} 1.0, SO_4^{2-} 0.5 mM) were nearly equal to those in human blood plasma. Before soaking in the SBF, the samples were ultrasonically washed in acetone for 10 min, and then sterilized in ethanol. The soaking took place in temperature control shaking water bath for various incubation times up to 4 weeks under physiological condition of pH 7.4 at 37.4 ± 0.1 °C. After the pre-selected soaking time, the samples were filtered, rinsed with deionized water and dried. The calcium ion concentrations of the solution were determined by ICP-OES, an average of 5 measurements were taken for each sample while typical standard deviation was in the range of 0.05–0.2 ppm. The changes in the pH value of the SBF were also measured.

The fluorine concentration released from the sample soaked in SBF was separately measured using a pF-meter (pH & ION meter GLP 22, Crison, Spain) with a fluoride-ion-selective electrode (I.S.I. Electrode, Code: 9655, Crison, Spain).

The apatite formation on the surface of the samples as a consequence of the dissolution and precipitation process of calcium phosphate was investigated by SEM.

3. Results and discussion

3.1. Phase structure analysis and optimization of MA parameters

Fig. 2(a–e) shows the XRD patterns of prepared FHA100 samples under milling conditions I–V, respectively (Table 1). The synthesizing time was 4 h for samples milled under conditions I and II, and 6 h for samples milled under conditions III, IV and V, respectively. Obviously, decreasing rotation speed of ball milling caused increasing the synthesizing time of FHA100 from 4 h under milling condition II to 6 and 10 h under milling conditions III and IV. Clearly, decreasing the powder to ball weight ratio from 35 under condition III to 20 under condition V, caused an increase in the synthesizing time of product from 6 to 15 h. By comparison between condition I and II, it could be observed that the number and size of balls had no significant effect on the synthesizing time when the rotation speed and powder to ball weight ratio were constant. In fact, the energy of each collision and the kinetic energy of the balls on impact with the powder particles were increased by increasing the size of balls from 1 cm under condition I to 2 cm under condition II as a result of increasing the mass of each ball but

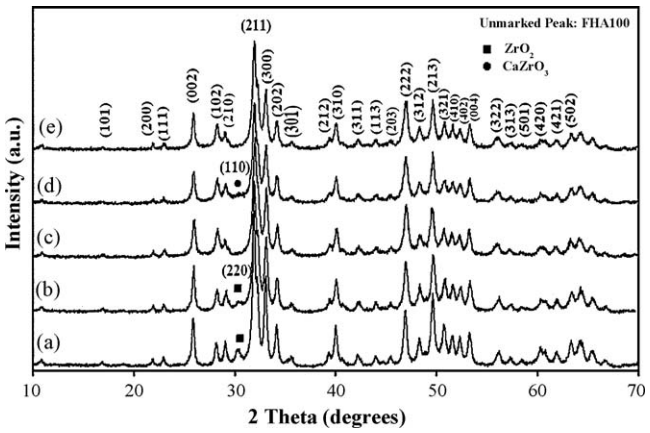

Fig. 2. XRD patterns of FHA100 samples after ball milling for: (a) 4 h under condition I, (b) 4 h under condition II, (c) 6 h under condition III, (d)10 h under condition IV and (e)15 h under condition V.

lower number of balls with larger size provided lower collision per unit time; consequently, the rate of FHA100 formation remained almost unchanged under condition I and II.

The XRD patterns (Fig. 2) indicated that a single-phase FHA100 with no impurity phase only was formed by performing ball milling process under conditions III and V. On the other hand, large amounts of ZrO_2 under conditions I and II, and $CaZrO_3$ under condition IV could be detected in product. It seems that lower reaction kinetic of reactant caused formation of $CaZrO_3$ as an impurity phase in the final obtained powder under condition IV according to Eq. (2).

$$Ca(OH)_2 + ZrO_2 \rightarrow CaZrO_3 + H_2O \quad (2)$$

The penalty of such a reaction was the consumption of the Ca from the final product [27]. Thus, the produced FHA100 phase after 10 h of milling under condition IV had the Ca/P ratio lower than stoichiometric value (Ca/P < 1.67) as a result of $CaZrO_3$ formation during milling under condition IV.

The effect of milling conditions and milling time under each condition on crystallite size of prepared FHA100 samples which was calculated using Williamson–Hall formula is shown in Fig. 3. By using the 350 rpm rotation speed, as a result of decreasing the numbers of balls from 12 under condition I to 8 under condition II, the crystallite size of synthesized powders showed a slight discrepancy only for 2 and 4 h of milling but upper than 4 h, the crystallite size was roughly equal under these two conditions and the graphs (a and b) followed a constant trend in terms of milling time after 4 h of milling. Also, the crystallite size increased because of decreasing the rotation speed or decreasing the powder to ball weight ratio.

It is well known that one of the most interesting features of mechanical alloying was its ability to produce nanostructure powders. Deformation strain during milling depends primarily on the radii and number of the balls and powder to ball weight ratio, which were used for mechanochemical treatment and the impact velocity number or stress cycles applied on the material. At the early stages of milling a dislocation cell structure was obtained which subsequently created low-angle grain boundaries. With prolonged processing, this structure

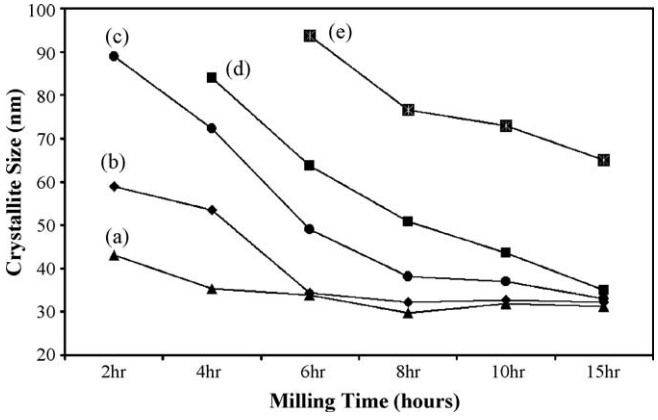

Fig. 3. The effect of milling conditions and time of milling on the crystallite size of FHA100 during milling under: (a) condition I, (b) condition II, (c) condition III, (d) condition IV, and (e) condition V.

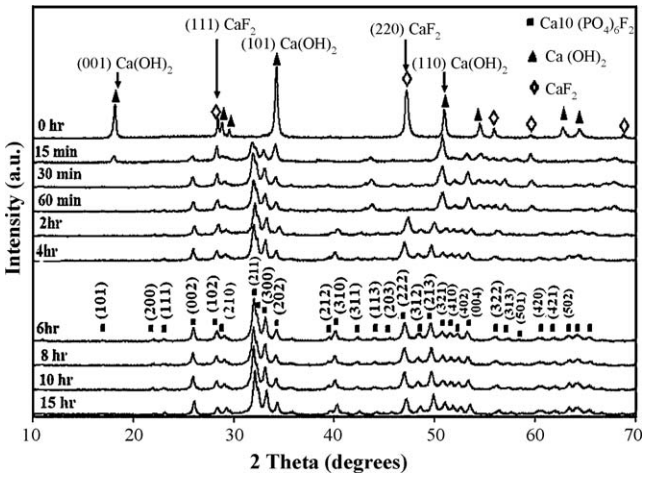

Fig. 4. XRD traces of initial $Ca(OH)_2$–P_2O_5–CaF_2 powder mixture after different milling times under condition III (FHA100 sample).

was transformed to fully nanocrystalline structure with completely random orientation of neighboring grains, which were separated by high-angle grain boundaries [21]. Thus, as a result of increasing the milling time, grain size decreases continuously until a saturation size is approached.

The XRD traces of initial powder mixture of FHA100 sample before and after different milling times under condition III are shown in Fig. 4. Only sharp characteristic peaks of $Ca(OH)_2$ and CaF_2 could be detected in XRD pattern of the initial powder mixture. The X-ray pattern of initial mixture showed that the most intense peaks of $Ca(OH)_2$ and CaF_2 disappeared at the early stages of milling after 2 h and 15 min, respectively. The X-ray traces of the samples which were milled for 15 min up to 4 h confirmed continuation of mechanochemical process. By increasing the milling duration up to 15 min, the emergence of both the broad and weak peaks around 31.7–33.5° indicated the formation of apatite phase and both broad envelope shape and weak intensity of peaks revealed that the newly formed apatite phase was poorly crystallized at the initial stages of milling, especially up to 1 h. Further increase in milling time up to 6 h resulted in further increase in crystalline order of the apatite phase-further sharpening of the principal diffraction peaks. The XRD traces from 15 min to 1 h showed that there were only two identified phases including apatite and calcium hydroxide. Based on XRD patterns, it could be concluded that the relatively well-crystalline fluorapatite (FHA100) was synthesized after 6 h of milling under condition III.

The "*d*" spacing of synthesized powder after 6 h of milling under milling condition III was compared with standard card of fluorapatite (JCDP #15-0876) and there was a good match with the standard both in terms of relative intensity and the position of the peaks. According to the XRD data, "*d*" value of the characteristic peaks, which have higher relative intensity than other peaks, were 0.2801, 0.27700, 0.27019 and 0.26235 nm for (2 1 1), (1 1 2), (3 0 0) and (2 0 2) Miller's planes, respectively, which had a good agreement with standard "*d*" values. These results could be an evidence that the fluoride ions entered completely into the crystal structure of apatite and formed

fluorapatite (FHA100) after 6 h of milling under condition III. The broadening of XRD peaks during milling up to 15 h occurred due to the reduction of the crystallite size as well as micro-strain induced in powder particles [21].

During the MA process, the deformation penetrates through the particle/particle assembly by means of dislocation mechanisms (sliding and climbing) of high velocity, i.e., via impact waves [28]. During mechanochemical process chemical and phase changes occurred due to the transfer of deformations with high elastic flow. Because of high elastic flow, the prevailing mechanism was creeping, while the specified changes could be completely irreversible. Critical creeping strain in the milling materials depends on the time that the system was exposed to deformation.

The trends of lattice strains of FHA0 and FHA100 samples milled under condition III, which were calculated using Williamson–Hall formula, in terms of milling time can be seen in Fig. 5. Clearly, the lattice strain of FHA100 milled sample decreased up to 6 h of milling; Afterwards, it increased as a result of increasing milling time up to 15 h. However, for FHA0 sample, the graph generally shows an upward trend at different milling times. Clarifying the subject, according to XRD traces of FHA100 sample at different milling times (Fig. 4); the fluorine-hydroxyl substitution into the apatite lattice started at the first stages of milling and, finally, after 6 h of milling the fluorapatite was synthesized. In other words, after 6 h of milling, fluorine ions completely incorporated into the apatite lattice instead of hydroxyl ions in the FHA100 sample. It seems that the lattice strain of FHA100 sample decreased during milling up to 6 h due to the fluorine ions with lower ionic radii (1.32 Å) than hydroxyl groups (1.68 Å) [18] incorporated into the apatite lattice instead of hydroxyl groups during milling up to 6 h and this substitution caused some contractions in the lattice. After 6 h of milling due to the complete incorporation of fluorine ions into the apatite lattice, no further fluorine substitution occurred and further milling caused high mechanical stress concentration over a very small contact area (contacts between the balls on their impacts or on impacts of the balls against inner walls). These phenomena provided conditions for the generation of high strain in the FHA100 milled powders; as a result, the graphs showed an upward trend after 6 h of milling. Obviously, since no fluorine ions incorporated in the lattice of FHA0 sample during milling, no contraction occurred in the lattice of apatite formed during milling; hence, the lattice strain of FHA0 sample increased during all stage of milling.

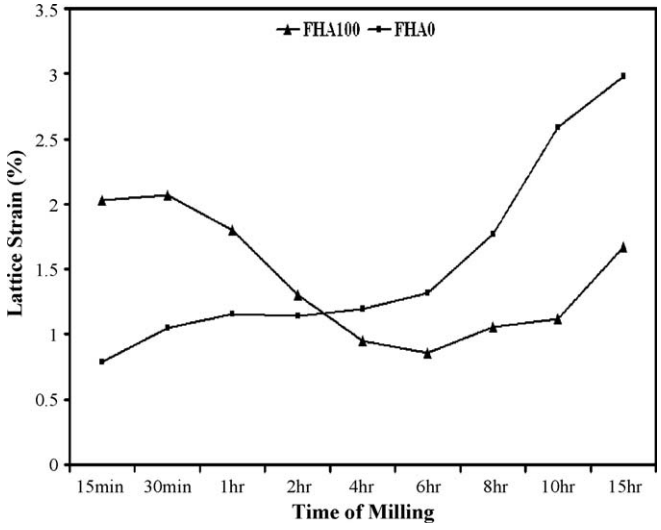

Fig. 5. The trends of FHA0 and FHA100 samples lattice strain in terms of milling time during milling under milling condition III.

XRD patterns of FHA0 and FHA100 powders subjected to MA for 6 h under condition III are shown in Fig. 6. No other peaks except for characteristic peaks of apatite were observed. By comparing the XRD pattern of FHA100 sample with FHA0 sample, it is clear that some set of FHA100 characteristic peaks (reflections) gradually shifted to the right hand side. The slight shift of characteristic peaks to the right side of the 2θ axis, which also was observed in other researches [9,13,14], was related to the decrease of the a-axis length of the hexagonal HA crystals lattice due to lower ionic radii of F^{1-} than OH^{1-} which caused introducing distortion in the lattice with incorporation of fluorine ions instead of hydroxyl groups in the apatite structure.

The lattice parameters and crystallite size of FHA0 and FHA100 samples calculated using XRD data, are shown in Table 2. Obviously, there were significant decrease in the a-axis from 0.9414 nm for FHA0 down to 0.9370 nm for FHA100 and, almost, similar values in the c-axis for these two samples were observed. These results are in a good agreement with slight shift of characteristic peaks in Fig. 6. Moreover, the crystallite size of FHA powders increased as a result of increasing fluorine content, which was also reported by Rodriguez-Lorenzo et al. [18]. The fluorine-hydroxyl substitution in the channel along the c-axis in the apatite structure explains why there is no change in cell parameter dimensions in the c-axis direction [8]. This fact, according to another report [29], could be evidence that all designed amount of fluoride in initial mixture enters into the apatite structure.

The lattice constant of pure FHA0 generally corresponded to the data reported by Key et al. [30]: $a = b = 0.9432$ nm and $c = 0.6881$ nm; a value just a little bit smaller. However a value was in good agreement with that of $a = 0.94155$ nm, reported by Wei et al. [20]. Also, the measured lattice constant values of FHA100 are very close to those reported by Wei et al. [20]: $a = b = 0.93716$ nm and $c = 0.6884$ nm.

3.2. TEM analysis

As it was mentioned before, according to the XRD data, the pure FHA100 phase only was synthesized under condition III

Table 2
Calculated lattice parameters and crystallite size of obtained powders subjected to MA for 6 h under condition III by using XRD data.

Sample	a-Axis (nm)	c-Axis (nm)	d (nm)
FHA0	0.9414	0.6881	41.482
FHA100	0.9370	0.6882	49.536

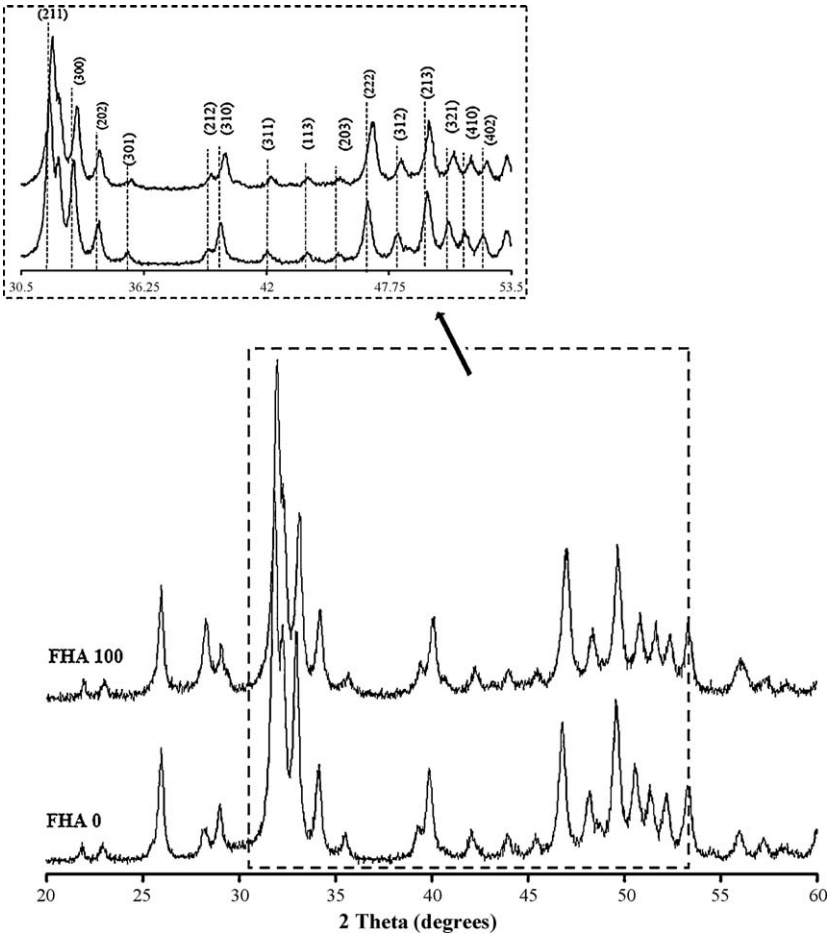

Fig. 6. XRD patterns of FHA0 and FHA100 milled samples for 6 h under milling condition III.

and V after 6 and 15 h of milling, respectively. Fig. 7 illustrated a detailed insight into the morphology of the FHA100 obtained powders after 6 h of milling under condition III (Fig. 7a–c) and 15 h of milling under condition V (Fig. 7d–f). According to Fig. 7a, nanosized particles, ~35–65 nm in size, had frequently polyhedron shapes with curved corners (Fig. 7b). In addition, it could be observed that some nanoparticles have needle-like shapes with, roughly, height of 70 nm and aspect ratio of 5 (Fig. 7c). It seems that the mean particle size of powder synthesized under condition V after 15 h of milling was larger than the mean particle size of powders synthesized under condition III after 6 h of milling. It is worth mentioning that the mean nanoparticle size measured using TEM micrographs for both samples was in a good agreement with the values calculated using Williamson–Hall formula and reported in Fig. 3.

3.3. Evaluation of powder purity

The concentrations of trace elements were reported as parts per million (ppm), whereas others followed with ASTM 1185-88 limits in brackets. The amounts of trace elements of milled powder under condition III (6 h milling) were determined as: As, 0.069(3); Cd, 0.052(5); Hg, 0.250(5); Pb, 0.824(30), and total amounts of Zr and other heavy metals, 45.900(50) where Zr concentration was exactly equal to 34.8 ppm. The trace elements concentrations of powder milled under condition V (15 h milling) were very close to those reported for the sample milled under condition III except the Zr concentration which was equal to 195.5 ppm. Other ions were not present in significant amounts and consequently, will not be considered further. Apparently, the produced powder which was milled for 6 h under condition III had high purity which could fulfill the requirements of ASTM 1185-88 standard to be used as a biomaterial but the Zr concentration of powder which was milled under condition V was clearly higher than the standard limit. Other powders which were milled under the other conditions (I, II, IV) obviously could not satisfy the requirement of standard specification due to the presence of impurity phase in their composition that was detected using XRD analysis and is obvious in Fig. 2.

According to these results, it could be concluded that, in comparison with other milling conditions (I, II, IV, V), condition III is the best milling conditions in order to produce high quality powders to be used as a biomaterial in biomedical applications. Therefore, in this research work, FHA0 nanopowder was synthesized under condition III to be compared with FHA100 sample especially in terms of in Vitro bioactivity. It should be mentioned that according to XRD data, which was discussed before, FHA0 nanopowder was synthesized after 6 h of milling under the milling condition III.

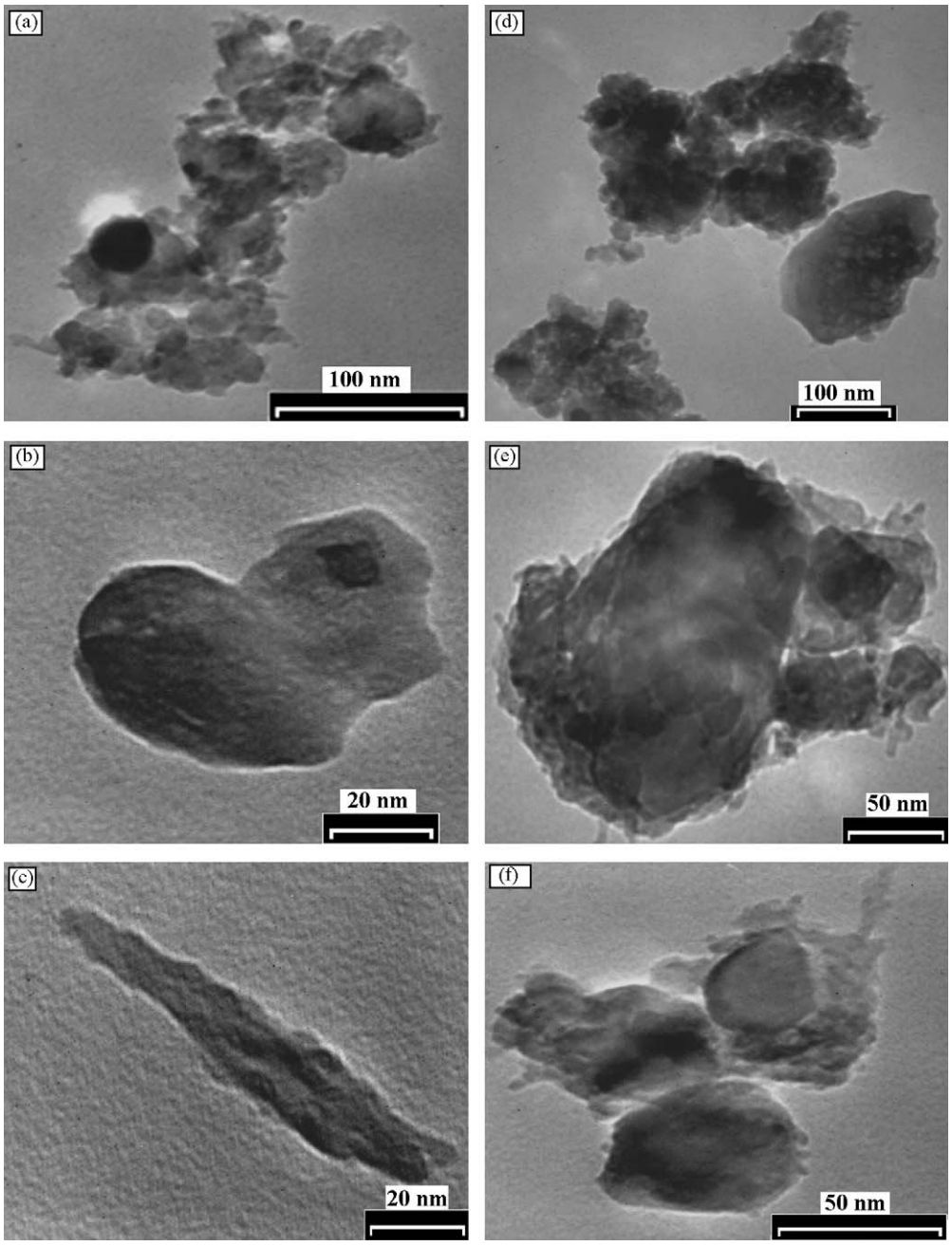

Fig. 7. TEM micrographs of the FHA100 samples after 6 h of milling under milling condition III (a–c) and 15 h of milling under milling condition V (d–f), which show the morphology and nanoparticle size distribution of the obtained FHA100 nanopowders.

3.4. FTIR analysis

FTIR spectra of $Ca(OH)_2$–P_2O_5–CaF_2 powder mixtures of FHA100 sample which were milled for different time under condition III are shown in Fig. 8. For the sample, which was milled for 0.5 h or longer, a doublet appears at 1420 and 1480 cm^{-1} corresponded to the v_3 and a band at 871 cm^{-1} corresponded to the v_2 stretching vibrations of the carbonate groups. It was suggested that the fluorapatite contained some CO_3^{2-} groups in PO_4^{3-} sites of apatite lattice (B-type substitution) [31]. This kind of apatite is more similar to biological appetites and could be more suitable for bone replacement materials. The characteristic peaks of PO_4^{3-} group which had four distinct asymmetrical stretching vibration modes namely v_1, v_2, v_3 and v_4 appeared in the broad spectrum. The v_1 and v_2 vibration peaks were observed at 961 and 471 cm^{-1}, respectively. As a major peak of phosphate group, the v_3 vibration peak was noticed in the region between 1100 and 1000 cm^{-1}, which was the most intensified peak among the phosphate vibration modes [32,33]. The band between 610 and 560 cm^{-1} indicated v_4 vibration mode of phosphate group, which occupied two sites in the crystal lattice each at 603 and 574 cm^{-1}. Two distinguishable splitting of v_4 vibrations were indicating the low site symmetry of molecules, as two peaks

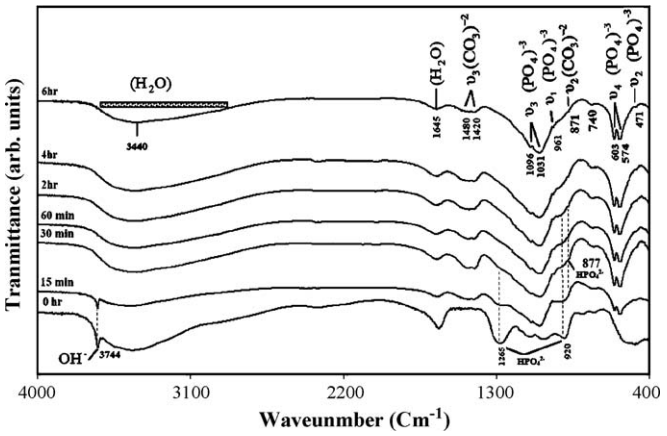

Fig. 8. FTIR spectra of the $Ca(OH)_2$–P_2O_5–CaF_2 powder mixture of FHA100 sample after different milling times under milling condition III.

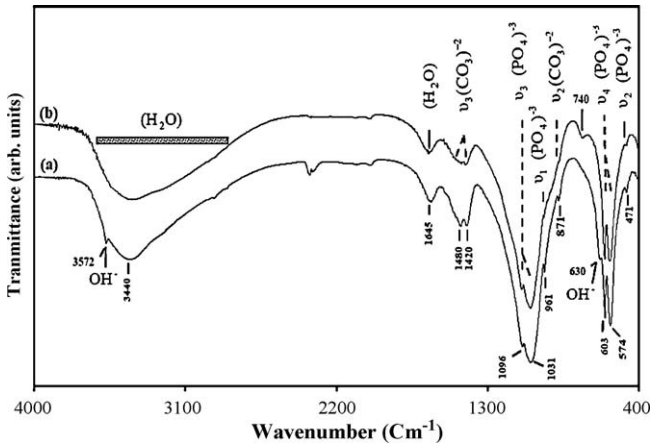

Fig. 9. FTIR spectra of the (a) FHA0 and (b) FHA100 nanopowders obtained after 6 h of milling under milling condition III.

confirmed the presence of more than one distinction site for the phosphate group in apatite lattice [33]. Comparing FTIR spectrum of the milled sample for 15 min with the spectrum of the starting mixture revealed a substantial change in the system phase composition, which occurred during the first 15 min of milling and had a good agreement with XRD trace in Fig. 4. As a result of milling continuation, appearance of a new band at 961 cm^{-1} and disappearance of the bands at 877, 920, 1265 and 3744 cm^{-1} were evident. The bands at 877, 920 and 1265 cm^{-1} assigned to the HPO_4^{2-} group vibrations [15] gradually diminished and finally disappeared after milling time longer than 4, 2 h and 30 min, respectively. It was reported that HPO_4^{2-} groups could easily substitute for phosphate ones in the apatite structure during the synthesis [34]. In the case of a sample which was milled longer than 60 min, the band at 961 cm^{-1} corresponding to the ν_1 vibration of the PO_4^{3-} group appeared as a result of the HPO_4^{2-} group depredation. Also, the band at 740 cm^{-1} corresponding to the shifting OH^- liberation mode appears after 30 min of milling and the intensity of this band increased with increasing milling time. Appearance of this band was caused by the increase of F^- content in the (OH^-, F^-) chain of apatite with predominant configuration of OH···F [18].

The FTIR spectrum of FHA0 and FHA100 synthesized powders are shown in Fig. 9. The spectrum of the FHA0 sample clearly showed bands corresponding to structural hydroxyl groups at 630 and 3572 cm^{-1} [32], suggesting fluoride ions incorporation into the apatite lattice for FHA100 sample. Both vibrations of the structural hydroxyl groups in the spectrum of the FHA0 sample depend on the strength of the hydrogen bonding system. The 3572 cm^{-1} is attributed to weakly hydrogen bonding while the 630 cm^{-1} is assigned to stronger hydrogen bonding. The fact of the matter is that these two vibrations at hydroxyapatite are due to OH^{1-} immersed in an infinite chain of OH^{1-} but this chain interrupted by F^{1-} in another compound (FHA100). As the fluoride ion incorporated into the apatite lattice, the bands assigned to the F···OH (740 cm^{-1}) appeared and the bands assigned to the structural OH^{1-} disappeared, significantly [18]. An interesting result, that is worthwhile to mention, is the absence of hydroxyl bands for fluorine-substituted hydroxyapatite. Some researchers [35] have neglected the existence of hydroxyl groups for mineral bone based on this absence while others [36] tend to believe that, in poorly crystalline appetites, hydroxyl groups are simply not resolved for several reasons. The results of the present study showed that there was enough coupling of the fluoride to mask the characteristic hydroxyl band. Based on the pervious report [37], there is also no evidence of bands that could be attributed to the OH···F···HO or OH···F···OH groups. In fact, after 6 h of milling, no characteristic bands of structural OH^{1-} at 3572 and 630 cm^{-1} and the presence of a band at 740 cm^{-1} could be evidence that all designed amounts of fluoride in initial mixture enter into the apatite structure [18].

According to the literature [37], the (OH^-, F^-) chain of apatite should contain at least three types of [OH^-] and a possible fourth one with distinguishable vibration energies: (1) the ''normal'' [OH^-] in an extended [OH^-] chain (configuration ···OHOHOH···), (2) ''tail to tail'' configuration HO:OH, (3) the F^- bonded [OH^-] in the symmetrical configuration ···OHFHO···, and finally (4) in F^- rich chains containing only a few [OH^-], in which the F^- bonded [OH^-] had an asymmetrical configuration ···FFOHFF···. In general, H, F apatite chains had ···FHO(OH)*n*HO:OH(OH)–*n*OHF··· configuration where *n* depends on OH^- and F^- ratio within the apatite. *n* decreased with increasing F^- ion content, and there was a ···FHOHO:OHOHF··· configuration for $n = 0$: with further increase of F··· vs. OH^- ion content in apatite, the chain reduces the number of OH^- ions until the formation of ···FHO:OHF··· and ···FOHF··· chain configuration.

3.5. SEM analysis

The SEM photomicrographs of FHA100 powder mixture after mechanical alloying for 2, 4 and 6 h of at two magnifications (2000× and 8000×) are shown in Fig. 10(a–f). Accumulated fine particles and laminate of polygonal shape were visible on the surfaces of larger particles. As a result of increasing the milling time, the size of these jointed fine particles on the surface of larger particles decreased, and the number of them increased, clearly.

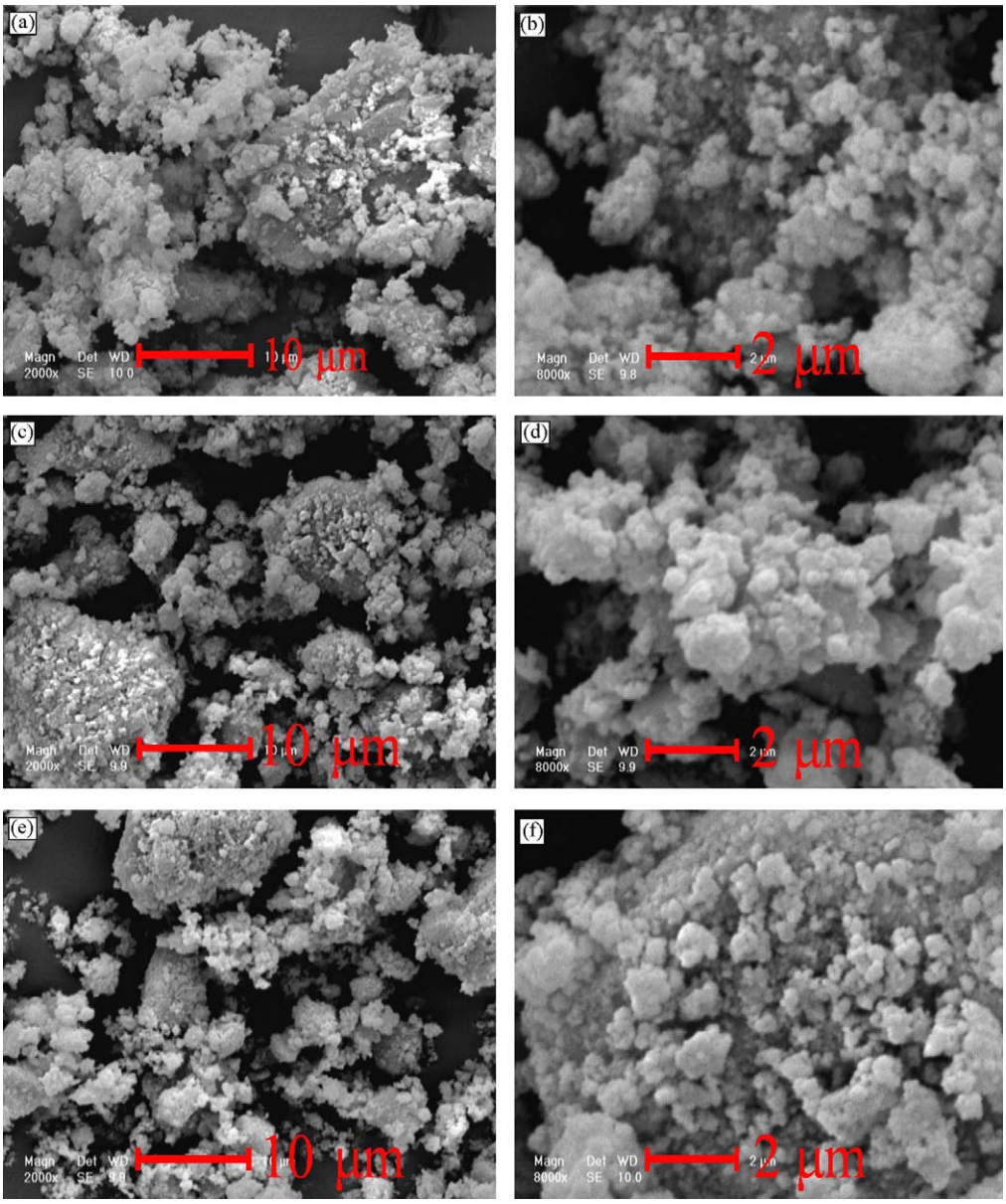

Fig. 10. SEM photomicrographs which show the morphology and agglomeration size distribution of the milled FHA100 samples after: 2 h (a and b), 4 h (c and d), 6 h (e and f) of mechanical alloying under milling condition III, at different magnifications.

3.6. In vitro bioactivity study

In order to investigate the effects of fluoridation on the in vitro bioresorbability and bioactivity of produced apatite nanopowders, FHA100 and FHA0 samples, which were synthesized after 6 h of milling under milling condition III, were immersed in the SBF and in vitro dissolution behavior of prepared FHA100 and FHA0 nanopowders were quantitatively examined in the SBF under physiological condition of pH 7.4 at 37.4 ± 0.1 °C at pre-determined time intervals up to 4 weeks.

The graph of the pH trends in terms of soaking time which illustrate the dissolution or bioresorbability behavior of synthesized FHA0 and FHA100 nanopowders can be seen in Fig. 11. The graph also shows the variation in pH with time for a SBF without any immersed powder in it, which acts as a control. The pH value is dependent on solubility or resorbability of the apatite, wherein the pH decrease as the solubility increases. It is apparent from the graph that the rate of bioresorbability of the FHA0 is higher than FHA100. Obviously, replacing OH^{1-} with F^{1-} ions in the apatite structure caused a drastic reduction in the apatite dissolution rate in the SBF.

The trends of calcium concentration in the SBF during soaking, also, were quantitatively estimated to support in vitro dissolution behavior of samples and results can be seen in Fig. 12. For both samples, during soaking in the SBF, the concentration of calcium ions in SBF increased, significantly. However, as a result of incorporating of fluorine ions into the apatite structure instead of hydroxyl groups, the increasing rate of calcium ion concentration of FHA100 is lower than FHA0 which is in good agreement with the pH variation of the solution during soaking in the SBF.

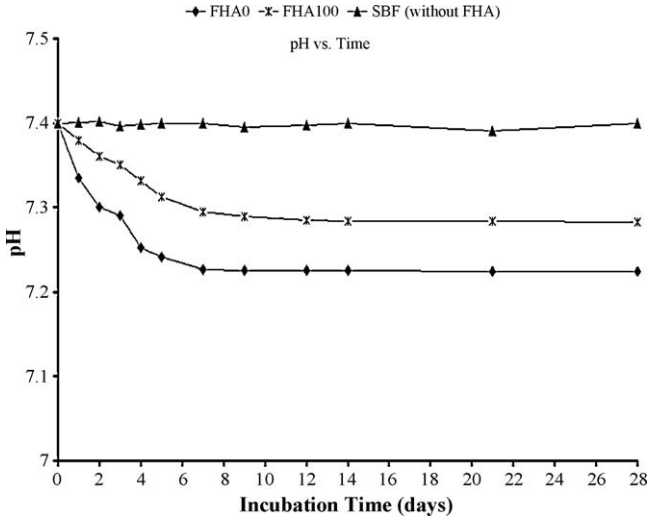

Fig. 11. pH values of SBF solution versus incubation time for FHA0 and FHA100 samples which were synthesized after 6 h of ball milling under milling condition III.

This phenomenon could be explained by considering the crystal structure of HA. According to the results of other researchers [8,9], the hydrogen (H^{1+}) ions of HA were arranged in the atomic interstices neighboring to the oxygen ions (O^{2-}) along the *c*-axis of apatite structure, forming OH^{1-} groups and were oriented randomly, which conferred a certain degree of disorder to the crystal structure of HA. Once the OH^{1-} groups were partially substituted by the F^{1-} ions, the existing hydrogen ions of the OH^{1-} groups were bound to the nearby F^{1-} ions because of the higher affinity of the F^{1-} ions compared to the oxygen ions, producing a quite well-ordered apatite structure, which caused an increase in chemical stability and a decrease in solubility of HA matrix. Therefore, when F^{1-} ions substituted the OH^{1-} groups in the HA matrix, a certain level of solubility resistance of the apatite ceramics was achieved.

Fig. 13 shows the release of fluorine ions from the fluoridated hydroxyapatite nanopowders immersed in SBF during soaking time. From the FHA0 sample, no fluorine was released

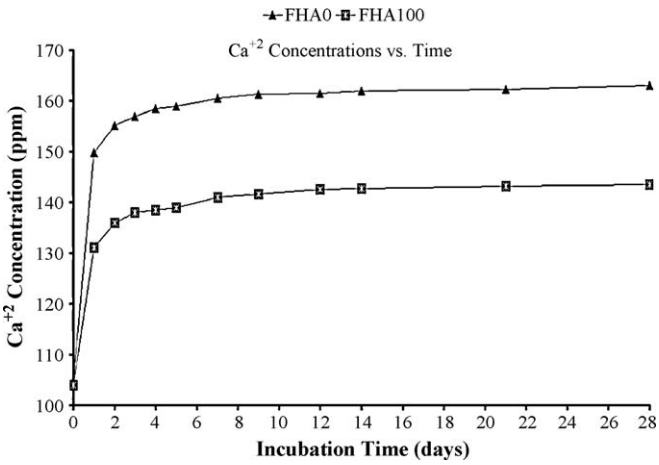

Fig. 12. Calcium ion concentrations of SBF solution versus incubation time for FHA0 and FHA100 samples which were synthesized after 6 h of milling under milling condition III.

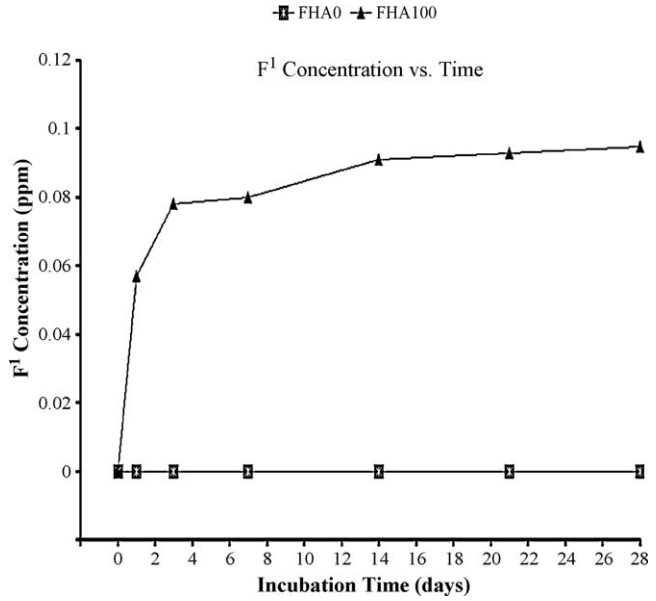

Fig. 13. Fluoride ion concentrations of SBF solution versus incubation time for FHA0 and FHA100 samples which were synthesized after 6 h of milling under milling condition III.

as expected. However, from the FHA100 sample, the fluorine ion was released during soaking in the SBF. Fluorine ion released almost with the rate of 2.59×10^{-2} ppm/day at the first 3 days of immersion but after that, the release rate was decreased to almost 6.792×10^{-4} ppm/day. It is reported that HA substituted with fluorine had higher osteoblastic cellular activity [38], and that micro-molar concentrations of fluorine were effective to stimulate cell proliferation and differentiation [39]. Regarding the exact concentration of fluorine, which is appropriate for cell response, there is still controversy over the range 10^{-5} to 10^{-7} M. The concentrations of fluorine released in this study were all within this range; hence, the FHA100 sample is consider releasing the optimal amount of fluorine for cellular activity.

The bone-like apatite formation on the surface of the FHA0 and FHA100 samples as a consequence of the dissolution and precipitation process of calcium phosphate was investigated by SEM. The morphology, size and amount of bone-like apatite crystals precipitated on the surface of FHA0 and FHA100 powders are shown in Fig. 14(a–h) and Fig. 15(a–h), respectively. SEM photomicrographs illustrate that bone-like appetites precipitated on the surface of each sample were mostly agglomerated. Furthermore, the average size and the number of agglomerated precipitates on the surface of each sample increased as a result of increasing incubation time. Apparently, in comparison with FHA100 sample, both quantity and size of precipitates formed on the surface of the FHA0 sample is higher at different soaking times. Moreover, the precipitates formed on the surface of the FHA0 sample are more agglomerated than the precipitates formed on the surface of the FHA100 sample, especially in higher soaking times.

It was well known that in the precipitation and crystallization processes from aqueous solutions, a competition bet-

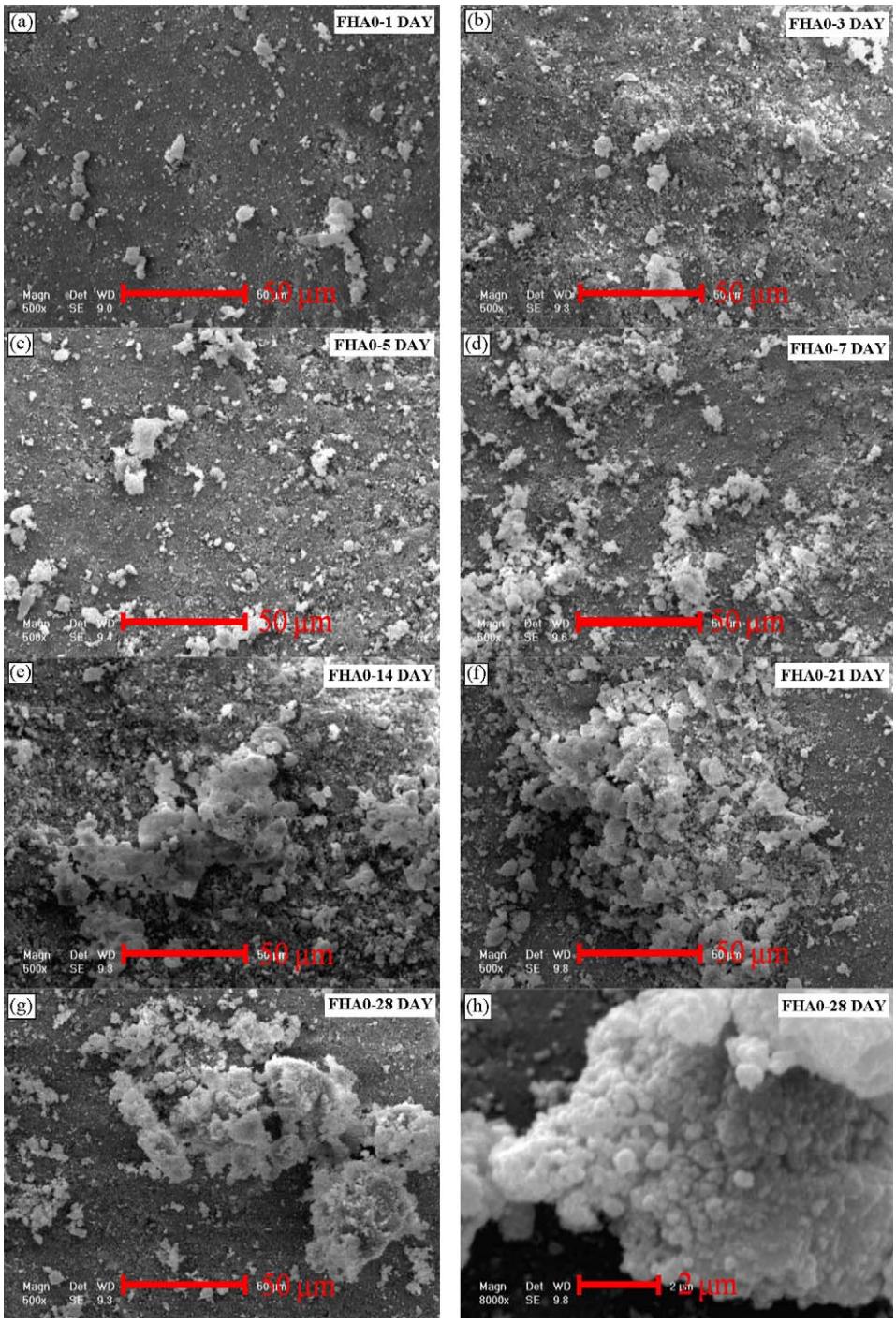

Fig. 14. SEM photomicrographs which show the morphology and amount of bone-like appetites formed on the surface of the FHA0 samples after: 1 day (a), 3-day (b), 5-day (c), 7-day (d), 14-day (e), 21-day (f) and 28-day (g and h) soaking in the SBF (samples were synthesized under milling condition III after 6 h of milling).

ween nucleation and crystal growth phenomena occurs that these phenomena could determine the size and morphology of the precipitated crystals in different saturation states. Moreover, this behavior could be explained by saturation state of the system that influences the growth process [40]. In fact, the higher solubility of FHA0 sample was the cause of increasing the super-saturation of the SBF solutions and initiating the subsequent precipitations since Ca^{2+} and PO_4^{3-} ions of solution in non-equilibrium conditions tend to migrate more easily to the solid/liquid interface, decreasing its free energy at higher super-saturation state of SBF. After 28 days of soaking, at higher magnification (Figs. 14 and 15, part h), it was evident that these agglomerates consist of many nanosized spherical particles. The size of these nanosized particles varied from 40 to 200 nm on the surface of FHA100 sample. But the average size of these precipitated particles on the surface of FHA0 sample was higher than FHA100, almost in the range of 180–400 nm.

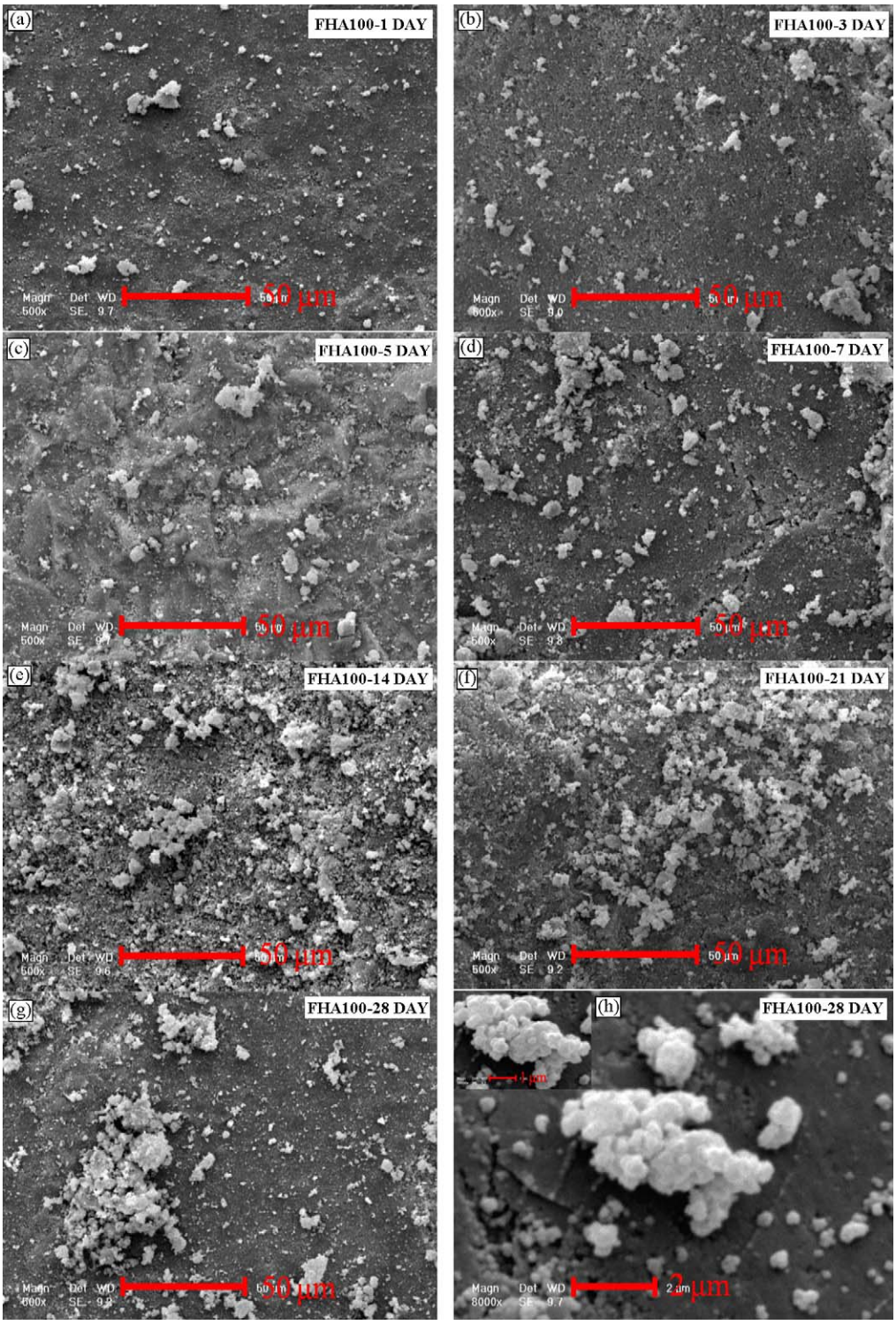

Fig. 15. SEM photomicrographs which show the morphology and amount of bone-like apatite formed on the surface of FHA100 samples after: 1 day (a), 3-day (b), 5-day (c), 7-day (d), 14-day (e), 21-day (f) and 28-day (g and h) soaking in the SBF (samples were synthesized under milling condition III after 6 h of milling).

4. Conclusion

(1) The obtained fluorapatite nanopowders which were synthesized by 6 h of milling under optimized mechanical alloying parameters including; 300 rpm of rotation speed, ball to powder weight ratio (B/P) equal to 35, and 8 balls with 20 mm in diameter, had high purity and could satisfy the requirements of ASTM 1185-88 standard to be used as a biomaterial in biomedical application.

(2) The size and number of balls had no significant effect on the synthesizing time and grain size of fluorapatite nanopowder when the rotation speed and powder to ball weight ratio

were constant while decreasing rotation speed or ball to powder weight ratio (B/P) increased synthesizing time and grain size of fluorapatite nanopowder during ball milling.
(3) Incorporation of fluorine ions into the apatite lattice instead of hydroxyl groups decreased the bioresorbability of apatite in the SBF and the quantity of precipitated bone-like apatite crystals on the surface of fluorapatite samples decreased compared to the hydroxyapatite during immersion in SBF.

Acknowledgement

The authors are grateful for support of this research by Isfahan University of Technology.

References

[1] C. Qiu, X. Xiao, R. Liu, Biomimetic synthesis of spherical nano-hydroxyapatite in the presence of polyethylene glycol, Ceram. Int. 34 (2008) 1747–1751.
[2] Y. Sun, G. Guo, Z. Wang, H. Guo, Synthesis of single-crystal HAP nanorods, Ceram. Int. 32 (2006) 951–954.
[3] S. Ramesh, C.Y. Tan, S.B. Bhaduri, W.D. Teng, Rapid densification of nanocrystalline hydroxyapatite for biomedical applications, Ceram. Int. 33 (2007) 1363–1367.
[4] G. Ye, T. Troczynski, Hydroxyapatite coatings by pulsed ultrasonic spray pyrolysis, Ceram. Int. 34 (2008) 511–516.
[5] B. Kim, J. Jeong, Y. Jeon, K. Jeon, K. Hwang, Hydroxyapatite layers prepared by sol–gel assisted electrostatic spray deposition, Ceram. Int. 33 (2007) 119–122.
[6] C. Kaya, Electrophoretic deposition of carbon nanotube-reinforced hydroxyapatite bioactive layers on Ti–6Al–4V alloys for biomedical applications, Ceram. Int. 34 (2008) 1843–1847.
[7] A. Balamurugan, G. Balossier, S. Kannan, J. Michel, J. Faure, S. Rajeswari, Electrochemical and structural characterization of zirconia reinforced hydroxyapatite bioceramic sol–gel coatings on surgical grade 316L SS for biomedical applications, Ceram. Int. 33 (2007) 605–614.
[8] L.L. Hench, J. Wilson, An Introduction to Bioceramics, World Scientific Publishing Co., Singapore, 1993.
[9] Y. Chen, X. Miao, Thermal and chemical stability of fluorohydroxyapatite ceramics with different fluorine contents, Biomaterials 26 (2005) 1205–1210.
[10] H. Kim, H.E. Kim, J.C. Knowles, Fluor-hydroxyapatite sol–gel coating on titanium substrate for hard tissue implants, Biomaterials 25 (2004) 3351–3358.
[11] H. Kim, Y. Kong, C. Bae, Y. Noh, H.E. Kim, Sol–gel derived fluor-hydroxyapatite biocoatings on zirconia substrate, Biomaterials 25 (2004) 2919–2926.
[12] K. Cheng, W. Weng, H. Qu, P. Du, G. Shen, G. Han, J. Yang, J.M.F. Ferreira, Sol–gel preparation and in vitro test of fluorapatite/hydroxyapatite films, J. Biomed. Mater. Res. Part B Appl. Biomater. 69E (2004) 33–37.
[13] B.H. Yoon, H.W. Kim, S.H. Lee, C.J. Bae, Y.H. Koh, Y.M. Kong, H.E. Kim, Stability and cellular responses to fluorapatite–collagen composites, Biomaterials 26 (2005) 2957–2963.
[14] K. Cheng, W. Weng, H. Wang, S. Zhang, In vitro behavior of osteoblast-like cells on fluoridated hydroxyapatite coatings, Biomaterials 26 (2005) 6288–6295.
[15] H. Zhang, Q. Zhu, Z. Xie, Mechanochemical–hydrothermal synthesis and characterization of fluoridated hydroxyapatite, Mater. Res. Bull. 40 (2005) 1326–1334.
[16] K. Cheng, S. Zhang, Sol–gel preparation of fluoridated hydroxyapatite in $Ca(NO_3)_2$–$PO(OH)_{3-x}(OEt)_x$–HPF_6 system, J. Sol–Gel Sci. Technol. 38 (2006) 13–17.
[17] E.Z. Kurmaev, S. Matsuya, S. Shin, M. Watanabe, R. Eguchi, Y. Ishiwata, T. Takeuchi, M. Iwami, Observation of fluorapatite formation under hydrolysis of tetracalcium phosphate in the presence of KF by means of soft X-ray emission and adsorption spectroscopy, J. Mater. Sci.: Mater. Med. 13 (2002) 33–37.
[18] L.M. Rodriguez-Lorenzo, J.N. Hart, K.A. Gross, Influence of fluorine in the synthesis of apatites. Synthesis of solid solutions of hydroxy-fluorapatite, Biomaterials 24 (2003) 3777–3785.
[19] H. Qu, M. Wei, Synthesis and characterization of fluoride-containing hydroxyapatite by a pH-cycling method, J. Mater. Sci.: Mater. Med. 16 (2005) 129–133.
[20] M. Wei, J.H. Evans, T. Bostrom, L. Grndahl, Synthesis and characterization of hydroxyapatite, fluoride-substituted hydroxyapatite and fluorapatite, J. Mater. Sci.: Mater. Med. 14 (2003) 311–320.
[21] C. Suryanarayana, Mechanical alloying and milling, Prog. Mater. Sci. 46 (2001) 1–184.
[22] L. Zhang, Z. Xu, Y. Feng, Y. Hu, X. Yao, Synthesis, sintering and characterization of PNZST ceramics from high-energy ball milling process, Ceram. Int. 34 (2008) 709–713.
[23] K. Park, J.G. Kim, K.J. Lee, W.S. Cho, W.S. Hwang, Electrical property and microstructure of Y-doped $BaTiO_3$ ceramics prepared by high-energy ball-milling, Ceram. Int. 34 (2008) 1573–1577.
[24] ASTM, Standard specification for composition of ceramic hydroxyapatite for surgical implants, ASTM 415 (1988) F1185–F1188.
[25] K. Williamson, W.H. Hall, X-ray line broadening from filed aluminium and wolfram, Acta Metall. 1 (1953) 22–31.
[26] T. Kokubo, H. Takadama, How useful is SBF in predicting in vivo bone bioactivity? Biomaterials 27 (2006) 2907–2915.
[27] C.Y. Chiu, H.C. Hsu, W.H. Tuan, Effect of zirconia addition on the microstructural evolution of porous hydroxyapatite, Ceram. Int. 23 (2007) 715–718.
[28] M.V. Chaikinain, E.G. Avvakumov (Eds.),Mehanohimija prirodnih i sinteticheskih apatitov, Novosibirsk, Izdatelstvo soran Filial "Geo" (2002).
[29] H.W. Kim, Y.J. Noh, Y.H. Koh, H.E. Kim, Enhanced performance of fluorine substituted hydroxyapatite composites for hard tissue engineering, J. Mater. Sci.: Mater. Med. 14 (2003) 899–904.
[30] M. Kay, R.A. Young, A.S. Posner, Crystal structure of hydroxyapatite, Nature 204 (1964) 3056–3065.
[31] S. Sasikumar, R. Vijayaraghavan, Solution combustion synthesis of bioceramic calcium phosphates by single and mixed fuels—a comparative study, Ceram. Int. 33 (2008) 1373–1379.
[32] C.Y. Ooi, M. Hamdi, S. Ramesh, Properties of hydroxyapatite produced by annealing of bovine bone, Ceram. Int. 33 (2007) 1171–1177.
[33] R. Murugan, S. Ramakrishna, Aqueous mediated synthesis of bioresorbable nanocrystalline hydroxyapatite, J. Cryst. Growth 274 (2005) 209–213.
[34] J.P. Lafon, E. Champion, D. Bernache-Assollant, Processing of AB-type carbonated hydroxyapatite$Ca_{10-x}(PO_4)_{6-x}(CO_3)_x(OH)_{2-x-2y}(CO_3)_x$ ceramics with controlled composition, J. Eur. Ceram. Soc. 28 (2008) 139–147.
[35] C. Rey, J.L. Miquel, L. Facchini, A.P. Legrand, M.J. Glimcher, Hydroxyl groups in bone mineral, Bone 16 (1995) 583–586.
[36] M.G. Taylor, S.F. Parker, K. Simkiss, C.H. Mitchell, Bone mineral: evidence for hydroxy groups by inelastic neutron scattering, Phys. Chem. Chem. Phys. 3 (2001) 1514–1517.
[37] F. Freund, R.M. Knobel, Distribution of fluorine in hydroxyapatite studied by infrared spectroscopy, J. Chem. Soc. Dalton Trans. 6 (1977) 1136–1140.
[38] R. Murugan, T. Kumar, K. Rao, Fluorinated bovine hydroxyapatite, preparation and characterization, Mater. Lett. 57 (2002) 429–433.
[39] J. Farley, J. Wergedal, D. Baylink, Fluoride directly stimulates proliferation and alkaline phosphates activity of bone-forming cells, Science 222 (1983) 330–332.
[40] C. Ribeiro, E.C.S. Rigo, P. Sepúlveda, J.C. Bressiani, A.H.A. Bressiani, Formation of calcium phosphate layer on ceramics with different reactivates, Mater. Sci. Eng. C 24 (2004) 631–636.